https://doi.org/10.5194/egusphere-2023-2220
Preprint. Discussion started: 13 November 2023

Drop Size Distribution Retrieval Using Dual Frequency Polarimetric Weather Radars

Daniel Durbin[1], Yadong Wang[1], and Pao-Liang Chang[2]

[1]Electrical and Computer Engineering Department, Southern Illinois University Edwardsville, Illinois, USA
[2]Central Weather Bureau, Taipei, Taiwan

Correspondence: Daniel Durbin (ddurbin@siue.edu)

Abstract. Having knowledge of the drop size distribution (DSD) is of particular interest to researchers as it is widely applied to quantitative precipitation estimation (QPE) methods. Polarimetric radar measurements have previously been utilized to derive DSD curve characteristics frequently modeled as a gamma distribution. Likewise, approaches using dual frequency measurements have shown positive results. Both cases have relied on the need to constrain the relationship between the DSD parameters based on prior knowledge or assumptions of the collected data. This paper presents a methodology for retrieving the DSD parameters using the dual frequency and polarimetric nature of measurements from a unique data set taken at co-located S-band and C-band dual polarization radars. Using the reflectivity and differential phase measurements from each radar, an optimization routine employing particle swarm optimization (PSO) and T-Matrix computation of radar parameters is able to accurately retrieve the gamma distribution parameters without the constraints required in previous methods. Retrieved results are compared to known truth data collected using a network of OTT PARSIVEL disdrometers in Taiwan in order to assess the success of this procedure.

1 Introduction

Knowledge of the Drop Size Distribution (DSD) for a given location is an incredibly valuable piece of information. The most accurate rainfall estimates can be achieved with an accurate assessment of the DSD. The applicability of deducing localized DSDs to Quantitative Precipitation Estimation (QPE) is evident. QPE provides society with many benefits. Being able to precisely identify or even forecast heavy precipitation can help emergency and water management services better deploy their services and can alert others of dangerous flash floods, which can ultimately save lives. The Drop Size Distribution (DSD) provides critical information about the composition of a given volume of atmosphere in a region of interest. It is expressed as the number of particles for each drop size given as an equivalent sphere with a reference diameter, typically measured in millimeters. By knowing the DSD, important measures such as reflectivity, rainfall rate, and total water content can be derived. These parameters are only as accurate as the DSD representation, which highlights the value of flexibility in the model.

The Marshall-Palmer distribution is a widely used model for describing the DSD of rain. It is based on an exponential distribution and assumes that the DSD is spatially and temporally homogeneous. The intercept parameter of the Marshall-Palmer distribution, which is set to 8000, determines the overall scale of the distribution. However, research has shown that

https://doi.org/10.5194/egusphere-2023-2220
Preprint. Discussion started: 13 November 2023

the Marshall-Palmer distribution is limited in its applicability to different types of precipitation and atmospheric conditions. Specifically, it has been found that the Marshall-Palmer distribution is only accurate in the stratiform precipitative region (Marshall and Palmer, 1948), which is a region of moderate, steady rainfall. As the rainfall rate increases and diverges from this mode of precipitation, the intercept factor exhibits a large degree of variability (Sauvageot and Lacaux, 1995). While it can be a useful approximation, it has limiations that should be taken into account when using it in applications such as QPE. A larger number of DSDs can be expressed generically in the form of a gamma function given by Equation 1 (Ulbrich, 1983).

$$N(D) = N_0 D^{\mu} \exp(-\Lambda D) \tag{1}$$

where $N(D)$ is the concentration for each diameter D (mm), and μ, Λ (mm^{-1}), and N_0 are the shaping parameter, the exponential slope parameter, and the initial concentration of the distribution, respectively. While the gamma DSD provides more flexibility than the exponential Marshall-Palmer distribution, its complexity can make it difficult to use for retrieval purposes, as three unknown parameters must be solved. In the past, researchers have attempted to simplify the process by assuming a relationship between these parameters.

Extensive research has been conducted to remotely estimate the drop size distribution (DSD), with many studies utilizing measurements taken at two frequencies. This is because using data from a single frequency is typically insufficient for accurately estimating the DSD and can only provide information about a single parameter at a specific location. (Meneghini et al., 1997). Gogucci and Baldini demonstrated this approach using Global Precipitation Measurement (GPM) dual wavelength radar measurements. The surface reference technique is used to calculate path-integrated attenuation for each frequency so that a set of reflectivity and attenuation integral equations is formed. The system can then be solved for the DSD parameters that best match the measurements. The disadvantage of the approach is that it relies on assuming μ is a function of the median volume diameter. (Gorgucci and Baldini, 2016)

Williams et al. (2014) also worked to show dual wavelength approaches could be performed with GPM data. The under-constrainment issue was overcome by creating a distribution of standard deviations of the mean drop diameter using a large number of surface disdrometer measurements. Superior results were achieved relative to approaches that assume μ is a constant in order to overcome the ill-constrained nature of the retrieval. (Williams et al., 2014). Many others have shown dual frequency measurements are exploitable for discerning these properties (e.g., Mardiana et al., 2004; Chandrasekar et al., 2005; Eccles, 1979; Kozu et al., 1991; Kummerow et al., 1989; Marzoug and Amayenc, 1994; Meneghini et al., 1992).

Attempts at retrieving DSD parameters utilizating dual polarization measurements have also been made. Brandes et al. used S-band measurements of reflectivity and differential reflectivity to seek the gamma parameters (Brandes et al., 2002). An empirical relation is assumed between μ and Λ. While this relationship was applicable to both convective and stratiform rains, it was localized to the Florida region of the United States which was used for study. Similar approaches using horizontal and differential reflectivity have also been successful in experiments in Central Oklahoma but still rely on constrained relationships of the parameters (Cao et al., 2010).

The aim of this work is to solve for the three variables of the gamma drop size distribution (DSD) without the need for additional constraints. To achieve this, measurements taken at two frequencies with both vertical and horizontal polarizations

https://doi.org/10.5194/egusphere-2023-2220
Preprint. Discussion started: 13 November 2023

are incorporated into optimization routines. This approach allows for the determination of DSD solutions that accurately represent the input reflectivity and phase information.

This paper is organized in the following manner. Section 2 conveys the methodology of this work. High-level design characteristics of the instruments used for data collection are provided, including the disdrometers and the two ground radars. Key elements of the data preprocessing routines are provided. Although details of the T-matrix method are beyond the scope of this paper, its use in conjunction with Ryzhhov's model is explained, including significant assumptions. The optimization approach is explained and compared to other possible strategies.

The results are demonstrated through several examples, comparing the disdrometer collected DSDs with the retrieved results from the proposed algorithm. In addition, a supplementary validation approach is discussed and demonstrated using the C-band reflectivity data that was not included in the proposed optimization routines. This approach serves as an external validation mechanism for the proposed algorithm and provides a comparison of the results obtained from the algorithm with those obtained from the C-band reflectivity data. The results demonstrate the effectiveness of the proposed algorithm in retrieving accurate DSDs and its potential usefulness in radar systems that utilize more than one frequency.

2 Methods

2.1 Instrumentation

In the current work, two co-located polarimetric radars, RCWF (S-band) and RCMD (C-band), are used in the algorithm development and validation. A photo of these two radars is shown in Figure 1, where RCWF and RCMD are located on the right and left panel, respectively. The Central Weather Bureau of Taiwan operates these two radars that provide real-time observations used for severe weather surveillance, quantitative precipitation estimation, hydrometeor classification, and precipitation microphysics studies. These radars play a critical role in monitoring and forecasting precipitation in Taiwan and provide key data that is useful in the research of preciptiative processes. The manufacturer models of RCWF and RCMD are the Weather Surveillance Radar 1988 Doppler (WSR-88D) and Gematronik, respectively. More technical specifications about these two radars can be found in Table 1. As shown in Figure 1, these two radars are adjacent to each other, and the distance between them is much less than the range resolution (250 m). Since these two radars have the same polarization and location, the divergence of the observed differential phase (Φ_{DP}) and reflectivity (Z) can therefore be attributable to only radar frequency difference. These measurement differences are the key variables implemented in the retrieval method.

To validate the performance of the proposed algorithm, DSD data collected by a laser-based optical system, the OTT Particle Size Velocity (PARSIVEL or Parsivel) Disdrometer, is used as the ground truth. The Prasivel disdrometer derives the DSD through the measured particle's size and velocity. There are 32 diameter and velocity bins available to measure particles with size between 0.062 mm to 24.5 mm and with velocity between 0.05 m s^{-1} to 20.8 m s^{-1}. The accuracy of Parsivel Disdrometer has been studied by Sheppard (2007); Jaffrain and Berne (2011).

Sampling with the OTT Parsivel may exhibit some degree of statistical variance, which is a common characteristic of all measurements. Microphysical events are inherently stochastic in nature and the physical sampling effects and noise also play

https://doi.org/10.5194/egusphere-2023-2220
Preprint. Discussion started: 13 November 2023

roles in the deviations (Sheppard, 2007). The Parsivel used in this dataset has been compared to more accurate 2D disdrometer data in order to gauge the variance. The findings of Jaffrain et al. demonstrated that sampling uncertainty is minimal for small to moderate drop sizes, but it starts to escalate for larger classes (greater than 2.0 mm). Notably, the data set used in this study lacks a large representation of drop sizes exceeding 2 mm, which is advantageous as the smaller class measurements can be assumed to be more accurate(Jaffrain and Berne, 2011).

Possible error sources of OTT Parsivel were investigated by Angulo-Martínez et al. (2018). It was found that uneven power distribution over the beamwidth or any time variation can adversely effect the accuracy. Other factors, such and the angle of the drop trajectory, coincidentally observed particles, and particles that intersect with only the edge will also lead to biases.

The locations of two dual polarization radars and OTT Parsivel disdrometers are depicted in Figure 2 with stars and circles, respectively. The complex terrain of Taiwan presents a significant challenge due to frequent radar beam blockage. The Central Mountain Range (CMR) is visible in Figure 2, running from the north to the south of the island, with the highest peak exceeding 3800 m. To mitigate the effects of vertical variability in radar measurements, only data from the two lowest unblocked tilts were used in the DSD retrieval. Additionally, two rings with ranges of 20 km and 70 km are shown in Figure 2. The performance of the proposed approach was validated only with the disdrometers located within these two ranges. More details related to the validation data selection will be provided in the following section.

2.2 Radar and Disdrometer Data

2.2.1 Preprocessing of Radar and Disdrometer Data

The Z and Φ_{DP} fields from both C- and S-band radars are the proposed parameters for DSD retrieval, and the qualities of both fields were examined and processed through a set of quality control procedures. The quality control process pertaining to the reflectivity field includes identifying and removing nonprecipitation radar echoes and smoothing along the radial direction. Any gate associated with correlation coefficient (ρ_{HV}) less than 0.98 was considered as likely produced by nonprecipitative clutter, and reflectivity is excluded from the average operation. The obtained reflectivity is then smoothed with a 4 km smoothing window along each radial direction. The raw Φ_{DP} field of RCMD was processed with the new Selex–Gematronik family of digital receiver and signal processor (GDRX) (Bringi et al., 2005). The GDRX processes the raw field using the field unwrapping, “good data” mask application, and finite impulse response (FIR) filtering. The details of the procedure can be found in Bringi et al. (2005). The similar procedure is also applied on the raw Φ_{DP} field from RCWF. Examples of processed reflectivity and differential phase fields are shown in Figure 3, where panels “a” (“c”) and “b” (“d”) show the reflectivity (raw differential phase) measured by S-band and C-band respectively. The yellow arrow in panel “a” indicates the radial path from the radars to the disdrometer location of interest. It should be noted the reflectivity fields from both frequencies show a similar trend, and the difference is mainly caused by the attenuation. The differential phase fields, on the other hand, show significant difference, which indicates that the differential phase is more sensitive to the radar frequency.

The DSD parameters are derived from the Parsivel disdrometer observations through the approach proposed by Raupach and Berne (Raupach and Berne, 2015). In this approach, information about individual raindrops, including their diameters, fall

https://doi.org/10.5194/egusphere-2023-2220
Preprint. Discussion started: 13 November 2023

velocities, and the effective sampling areas of the instrument was recorded. The drops are binned into diameter classes, and the concentration is then calculated through

$$N_i = \frac{1}{\Delta D_i \Delta t} \sum_{j=1}^{M} \frac{1}{S_j V_j} \tag{2}$$

where N_i is the drop concentration for the ith equivolume diameter class, S is the effective sampling area, V is the particles velocity, and ΔD_i and Δt are the class width and sampling period, respectively.

2.2.2 Data selection

The algorithm development and validation for RCWF and RCMD were based on nine days of data. These days included June 1, 2017, June 11-16, 2017, January 7, 2018, and May 7, 2018, during which light to moderate precipitation was observed in the region covered by the two radars. These days provided data representative of multiple precipitation intensities. One challenge in using both RCWF and RCMD is that they operate under different volume coverage patterns (VCPs). As a result, there is a slight time lag between scans from these two radars when observing the same location. To minimize the retrieval biases caused by the DSD variation during the time lag, the time stamp differences between scans from the two radars were limited to within one minute. This time limitation helped ensure that the retrieved DSD was as accurate as possible, given the time lag between the two radars.

In this work, the differences in both reflectivity and differential phase fields obtained from the S-band and C-band radars play critical roles in the DSD retrieval. The use of both S-band and C-band radars is necessary because the differing wavelengths allow for more accurate estimation of the DSD. The differences between the reflectivity and differential phase fields from both radars provide important information about the size distribution of the hydrometeors.

It is important to note that sufficient differences are expected from the two frequencies, specifically differential phase, in order to accurately estimate the DSD. If the differences are too small, it may result in a biased or inaccurate retrieval of the DSD. Thus, it is crucial to carefully select the observation range and ensure that there are sufficient differences in the fields to obtain an accurate DSD estimation. Another important factor to consider is that biases in the retrieved DSD can accumulate along the range. This means that the farther the distance between the radar and the target area, the larger the error in the retrieved DSD. This range effect is a predictable issue in radar data processing, and it underscores the importance of carefully selecting the range of interest when estimating the DSD. To achieve reasonable results, the following criteria for candidate data was therefore used:

- Range>25 km and Range<100 km
- $Z^S > 25$ dB

This set of criteria is designed to strike a balance between creating sufficient deviation between C and S band differential phases for an accurate DSD retrieval, while also preventing excessive error accumulation. Additionally, a reflectivity threshold of 25 dB is imposed to ensure that there is enough observable precipitation in the terminal gate.

https://doi.org/10.5194/egusphere-2023-2220
Preprint. Discussion started: 13 November 2023

Figure 3 illustrates an example of the raw Z data captured by the S-band and C-band radars with the location of the disdrometers indicated using black circles. Panels "a" and "b" show the reflectivity data obtained by the S-band and C-band radars, respectively. The yellow arrow in panel "a" indicates the radial path extending from the radars to the location of interest, where the disdrometer is also located, and the DSD along this radial is retrieved. Panels "c" and "d" display the raw Φ_{DP} fields gathered by the S-band and C-band radars. The Φ_{DP} information is critical to accurately retrieve the drop size distribution in the study as it serves as the primary source of independent inputs. This figure serves as a visual representation of the data used in the DSD retrieval algorithm and demonstrates the differences in the data between the S-band and C-band radars. Figure 4 shows the post-processed Z (panel "a") and Φ_{DP} (panel "b") fields along the yellow arrow of Figure 3. The measurements from S- and C-band radar are shown with blue and red color, respectively.

2.3 Drop size distribution with an artificial intelligence method

The flowchart of the proposed DSD retrieval algorithm is presented in Figure 5. Three variables of S-band reflectivity ($Z^S(r,\theta)$), and differential phase from both S- and C-band ($\phi^S_{DP}(r,\theta)$, $\phi^S_{DP}(r,\theta)$) are implemented as inputs, where r and θ are the coordinate of range and azimuthal angle, respectively. The analysis exclusively employed S-band reflectivity as it was considered a more dependable variable than Z^C in the dataset. The exclusion of Z^C was prompted by the potential to introduce more inaccuracies into the procedure due to the radar's heightened vulnerability to attenuation and uncertainty in calibration precision. Since Z^C displays high correlation with Z^S, it is unlikely that the inclusion of C-band reflectivity would furnish any additional useful insights into the retrieval. Moreover, the exclusion of Z^C from the process serves as an additional validation parameter, as discussed further in Section 3.

The radar variables from a given gate are first preprocessed with the routine described in Section 2.2.1, and the processed data are then used to retrieve three parameters as described in Section 2.3.2.

2.3.1 T-Matrix Computation of Radar Parameters

In the retrieval procedure, a set of DSD parameters in Equation 1 are first initialized within commonly observed ranges of the parameters (Zhang et al., 2001):

- $10^2 < N_0 < 10^{10}$
- $-2 < \mu < 10$
- $0 < \Lambda < 15$

With the initial parameters, the DSD ($N(D)$) is calculated, and radar variables of Z^S, K^S_{DP} (K^C_{DP}) and specific attenuation (A) are then calculated with the following equations:

$$Z = \frac{4\lambda^4}{\pi^4 |K_w|^2} \int_0^\infty |f_a(\pi)|^2 N(D) dD \tag{3}$$

https://doi.org/10.5194/egusphere-2023-2220
Preprint. Discussion started: 13 November 2023

$$K_{DP} = \frac{0.18\lambda}{\pi} \int_0^\infty \mathrm{Re}\{f_a(0) - f_b(0)\} N(D) dD \tag{4}$$

$$A = 8.686 \times 10^{-3} \lambda \int_0^\infty \mathrm{Im}\{f_b(0)\} N(D) dD \tag{5}$$

In the above equations, backscattering amplitudes, $f_a(0)$ ($f_a(\pi)$) and $f_b(0)$ ($f_b(\pi)$), at horizontal and vertical polarizations were calculated with the T-Matrix method (Waterman, 1965), where 0 and π indicate forward and backward scattering amplitude, respectively. The canting angle corresponding to the calculated amplitudes was zero, and the dielectric constant of water was referenced at 10 degrees Celsius.

With the obtained K_{DP} field, the Φ_{DP} field from both S- and C-band radar were then calculated through Equation 6, where ΔR represents the range difference between the ith gate and the previous gate.

$$\Phi_{DP}(r_i, \theta) = K_{DP} \Delta R + \Phi_{DP}(r_{i-1}, \theta) + \Phi_{DP}^{sys} \tag{6}$$

where Φ_{DP}^{sys} is the minimum system Φ_{DP}, and Φ_{DP}^{sys} for both radars could be found from Table 1.

2.3.2 Optimization Routine

The estimation of radar variables can be achieved by adjusting the DSD parameters in order to reduce the difference between the estimated and observed values. As this difference decreases, the optimization problem gradually approaches a minimum value, ultimately resulting in the retrieval of the desired information. Essentially, the retrieval problem can be considered as an optimization problem where the goal is to find the optimal set of parameters that minimize the difference between the estimated and observed values.

Multiple methods exist for minimizing the error between the simulated radar variables and the measured variables. A relatively simple approach that was first used is the Gauss-Newton method. While it can quickly converge on a solution, the technique will often only find local minima rather than the global minimum of the solution space. Another early attempt used the genetic algorithm (GA), which very reliably found better solutions. The GA, however, was very computationally intensive and relied on fine-tuning of the crossover and mutation factors to efficiently solve for the DSD.

Particle Swarm Optimization (PSO) was ultimately used for this work since it is comparatively more efficient at seeking the most representative DSD. Figure 6 shows the organization of the PSO application. For a gate with preprocessed reflectivity and differential phase measurements, particles with random N_0, μ, and Λ are initialized. Ranges for the particle positions were chosen according to commonly observed intervals (Zhang et al., 2001).

The three coordinates of each particle position collectively define a DSD that is used to calculate Z^S and $\Phi_{DP}^{S,C}$. Various cost functions which measure the distance from the preprocessed truth data were tried. The fitness function given by Equation 7 allows for relative weightings to be applied to each variable. Experimentally determined values ($\alpha = 5$, $\beta = \gamma = 1$) led to reliable retrievals. It should also be noted that Z^S is expressed as a logarithmic value rather than in linear units.

https://doi.org/10.5194/egusphere-2023-2220
Preprint. Discussion started: 13 November 2023

$$\text{Cost} = \alpha \left| \frac{Z^S_{\text{simulated}} - Z^S_{\text{measured}}}{Z^S_{\text{measured}}} \right| + \beta \left| \frac{\Phi^S_{DP,\,\text{simulated}} - \Phi^S_{DP,\,\text{measured}}}{\Phi^S_{DP,\,\text{measured}}} \right| + \gamma \left| \frac{\Phi^C_{DP,\,\text{simulated}} - \Phi^C_{DP,\,\text{measured}}}{\Phi^C_{DP,\,\text{measured}}} \right| \tag{7}$$

The cost of every particle is calculated, and the iteration's current best solution as well as the global best solution of all iterations are recorded. The particle positions are then updated according to Equation 8 where α is the local acceleration factor, β is the global acceleration factor, and r_1 and r_2 are random numbers between zero and one that are generated for each particle. This allows the particles to move towards the current and global best solutions and possibly find better solutions along the path. The convergence speed must be weighed against the possibility of "over-shooting" viable candidate solutions. α and β were determined experimentally, and values of 0.15 and 0.0015 were used for processing the overall data set.

$$\begin{bmatrix} N_0 \\ \mu \\ \Lambda \end{bmatrix}_{i+1} = \begin{bmatrix} N_0 \\ \mu \\ \Lambda \end{bmatrix}_{i} + \alpha \left\{ \begin{bmatrix} N_0 \\ \mu \\ \Lambda \end{bmatrix}_{\substack{\text{iteration} \\ \text{best}}} - \begin{bmatrix} N_0 \\ \mu \\ \Lambda \end{bmatrix}_{i} \right\} r_1 + \beta \left\{ \begin{bmatrix} N_0 \\ \mu \\ \Lambda \end{bmatrix}_{\substack{\text{global} \\ \text{best}}} - \begin{bmatrix} N_0 \\ \mu \\ \Lambda \end{bmatrix}_{i} \right\} r_2 \tag{8}$$

The swarm consisted of five thousand particles which were allowed four hundred iterations for each retrieval. A stability or minimum error criteria could easily be implemented to halt the retrieval that is displayed in Figure 6.

2.3.3 Retrieval Along Radial

The ultimate goal of the retrieval process is to obtain the DSD for the specific disdrometer location. To accomplish this, the PSO retrieval algorithm is applied to each location, starting from the one nearest the radar. The input reflectivity of the final gate must take into account any attenuation experienced between the radar and the disdrometer gate. Once a representative DSD is obtained for a gate, the attenuation is calculated, and the reflectivity for the next farthest gate is adjusted accordingly. This iterative process continues at 4 km intervals until the retrieval is performed at the terminal gate at the disdrometer location. This process is illustrated in Figure 7. By iteratively refining the DSD retrieval and adjusting the reflectivity for each gate, the algorithm effectively accounts for the changes in reflectivity due to attenuation along the path and provides an accurate representation of the DSD at the specific disdrometer location. Specifically, the radial-based approach used in this study involves starting with the first gate from each radial, which is assumed to be unattenuated. The measured reflectivity and differential phase are then directly input into the PSO algorithm to obtain the optimized DSD for this gate. For the next gate, the attenuation is calculated using the DSD from the previous gate and accounted for in the retrieval process. The true reflectivity for each gate is the measured reflectivity plus the attenuation calculated using the previously retrieved DSD. This process continues until the gate with the disdrometer is reached, at which point the final retrieval is performed

https://doi.org/10.5194/egusphere-2023-2220
Preprint. Discussion started: 13 November 2023

3 Performance Evaluation

The current study did not conduct a rigorous statistical analysis due to the limitations of the data, including the requirement for tightly synchronized observations from the radar. Instead, the primary aim was to demonstrate proof of concept and prototype the methodology for future studies that would incorporate a more systematic statistical analysis. While the results of the current study are promising, further work is needed to evaluate the accuracy and robustness of the proposed approach. A more comprehensive statistical analysis could be performed in the future to further validate the method and identify any potential sources of error. Nine days of data from 2017 and 2018 is used in the performance validation in the current work.

Therefore, the performance of the proposed approach is validated through qualitatively comparing the DSD obtained from the proposed approach and calculated from the disdrometer data. In panels A, B, and D, the disdrometer station with the identifier 466950 was located 69 km away from the radar and recorded terminal reflectivities of 42, 38, and 42 dBZ, respectively. For panel C, the disdrometer station with the identifier 467571 was situated 82 km away from the radar and recorded a terminal reflectivity of 38 dBZ.

Figure 8 shows four such representative examples of the algorithm results.

From Figure 8, it is noteworthy that the retrieved DSD fits drop sizes greater than 1 mm better than the region corresponding to smaller sizes. This can be due to two reasons. First, the radar cross section, which depends on the physical cross section, is simply smaller and will therefore affect the reflectivity and phase inputs less than the larger drops. This is also seen by inspection of Equations 3 and 4 where the integration or summing of the contribution of each size bin is clearly less for any decreased value of D. The second attributing factor is that the disdrometer measurements are unreliable at smaller drop sizes. A previous experimental evaluation of disdrometer accuracy across the drop spectra suggested 0.6 mm is the first reliable drop size determined by optical disdrometers (Tokay et al., 2001). Tokay's study also confirmed the first assertion in that the inaccuracy of small drop size measurements did not noticeably affect reflectivity measurements or DSD-derived metrics such as rain rate and attenuation. While some researchers have proposed that the goal of a retrieval should be to fit the prodominance of the size spectrum (Adirosi et al., 2013), it is clearly more important to represent medium to large diameters when the integral properties are the focus.

The role of the additional frequency in providing extra information is a key question addressed in this study. To investigate this, the retrieval algorithm was applied to select cases with the contribution of the C-band reflectivity excluded from the analysis. This exclusion was achieved through modification of the cost function in Equation 9 ($\alpha = 5$ and $\beta = 1$ were again chosen). The aim was to determine if both frequency bands were necessary to obtain accurate retrievals of the DSD.

$$\text{Cost} = \alpha \left| \frac{Z^S_{\text{simulated}} - Z^S_{\text{measured}}}{Z^S_{\text{measured}}} \right| + \beta \left| \frac{\Phi^S_{DP,\,\text{simulated}} - \Phi^S_{DP,\,\text{measured}}}{\Phi^S_{DP,\,\text{measured}}} \right| \tag{9}$$

Figure 9 shows the results of the algorithm applied with Equation 9 to the same scenario as the first case in Figure 8. Using two radar bands clearly increases the accuracy of the fit in this example. It is highly unlikely using a single frequency could produce comparably favorable results since no examples of DSD retrieval techniques using one wavelength were found in the literature which did not rely on a $\mu-\Lambda$ relationship or other constraint. Therefore, an exhaustive comparison of the performance

https://doi.org/10.5194/egusphere-2023-2220
Preprint. Discussion started: 13 November 2023

between the dual frequency and S-band only cases was not conducted, but several of these spot checks such as shown in Figure 9 were produced.

To ensure the accuracy of the retrieval algorithm, one can utilize the C-band parameters obtained from the retrieved DSDs to validate the S-band parameters. To accomplish this, the attenuation that is calculated from the retrieved DSDs can be applied to correct the C-band reflectivities affected by the large attenuation experienced over the path. However, the phase of the C-band return is less susceptible to attenuation and can be used as a useful tool for validating the retrieval algorithm.

Figure 10 suggests that the S-band reflectivity is relatively unaffected by attenuation as expected. The blue circles in the plot represent the raw reflectivity values measured by the S-band radar, which demonstrate the relatively low attenuation at this wavelength. The blue triangles in the plot represent the attenuation-corrected reflectivity values measured by the S-band radar.

The corrected C-band reflectivities are shown with red triangles in the plot and are seen to match well with the S-band values. This indicates that the correction factor derived from the retrieved DSD is effective in converting the C-band reflectivities to equivalent S-band values. By using this correction factor, we can confirm that the retrieved DSD accurately predicts the atmospheric effects at both radar bands.

4 Conclusions

A novel approach to retrieving the DSD using PSO has been discussed. While the retrieval is unconstrained regarding the gamma distribution parameters, the price is the additional data needed. The authors feel that radar systems utilizing more than one frequency will continue to become more commonplace. The value of dual polarization in radars is already universally accepted. Algorithms such as the one prototyped in this work will become more valuable as radar systems produce data with this type of increased diversity.

There are several limitations in this research which have been briefly mentioned and which future work should address. As stated, a statistical approach for evaluating the fitness of the DSDs and algorithm as a whole is needed. Excluding unreliable drop diameters may be a necessary step in any future rigorous evaluation methodology.

A larger dataset or preprocessing criteria should be assessed for long-term evaluation of the approach. While ten days of data were screened, the selection process for useful cases was highly discriminatory. Only measurements from the two radars which were synchronized within two minutes and identical in elevation angle became candidates. Of these, only data with corresponding disdrometer truth data and minimum terminal gate reflectivity were included in the processing pool. Preprocessing the measurements led to the greatest reduction in potential data. The majority of these cases were excluded because of data quality, in most cases due to unreliable phase profiles. Future work should exhaustively assess the approach by processing a larger amount of high quality data.

One focus of this project was to show that N_0, μ, and Λ are independently solvable when incorporating both multi-frequency and multi-polarization information. Restricted relationships between the variables are still highly useful. If the intended use of any retrieval algorithm can utilize a constraint with high confidence, the DSD retrieval process becomes much more efficient.

https://doi.org/10.5194/egusphere-2023-2220
Preprint. Discussion started: 13 November 2023

The tradeoff is that shaping characteristics may not be captured which is why study of more flexible retrieval processes should continue.

The optimization approach involves various adjustable parameters, including swarm size, number of iterations, and acceleration coefficients. Fine-tuning these parameters could result in faster and more optimal results. Moreover, adapting the algorithm to function as an embedded application for field testing is also a promising area for further development.

Code and data availability.

The datasets and source code used in this study are available from the corresponding authors upon request (ddurbin@siue.edu or yadwang@siue.edu).

Author contributions.

Dr. Yadong Wang and Daniel Durbin conceived the original idea of using dual frequency, dual polarization measurements for DSD retrieval and prototyped initial algorithms to show proof of concept. Daniel Durbin further applied the PSO technique, processed the data set, and prepared the draft of this paper. Both authors collaborated on the development of the final algorithm. Dr. P.-L. Chang provided and processed radar data from CWB and was further involved in algorithm discussion and article authoring.The Central Weather Bureau of Taiwan provided the unique data used in the project.

Competing interests.

The authors declare that there is no conflict of interest.

Acknowledgements. The authors thank the radar engineers at CWB for helping collect and process the radar data used in the study.

https://doi.org/10.5194/egusphere-2023-2220
Preprint. Discussion started: 13 November 2023

References

Adirosi, E., Baldini, L., Lombardo, F., Russo, F., and Napolitano, F.: Comparison of different fittings of experimental DSD, in: AIP Conference Proceedings, AIP, https://doi.org/10.1063/1.4825850, 2013.

Angulo-Martínez, M., Beguería, S., Latorre, B., and Fernández-Raga, M.: Comparison of precipitation measurements by OTT Parsivel^2 and Thies LPM optical disdrometers, Hydrology and Earth System Sciences, 22, 2811–2837, https://doi.org/10.5194/hess-22-2811-2018, 2018.

Brandes, E. A., Zhang, G., and Vivekanandan, J.: Experiments in Rainfall Estimation with a Polarimetric Radar in a Subtropical Environment, Journal of Applied Meteorology, 41, 674–685, https://doi.org/10.1175/1520-0450(2002)041<0674:eirewa>2.0.co;2, 2002.

Bringi, V. N., Thurai, M., and Hannesen, R.: Dual-Polarization weather radar handbook, 2nd ed. Neuss, p. 163 pp, 2005.

Cao, Q., Zhang, G., Brandes, E. A., and Schuur, T. J.: Polarimetric Radar Rain Estimation through Retrieval of Drop Size Distribution Using a Bayesian Approach, Journal of Applied Meteorology and Climatology, 49, 973–990, https://doi.org/10.1175/2009jamc2227.1, 2010.

Chandrasekar, V., Li, W., and Zafar, B.: Estimation of raindrop size distribution from spaceborne Radar observations, IEEE Transactions on Geoscience and Remote Sensing, 43, 1078–1086, https://doi.org/10.1109/tgrs.2005.846130, 2005.

Eccles, P. J.: Comparison of Remote Measurements by Single- and Dual-Wavelength Meteorological Radars, IEEE Transactions on Geoscience Electronics, 17, 205–218, https://doi.org/10.1109/tge.1979.294650, 1979.

Gorgucci, E. and Baldini, L.: A Self-Consistent Numerical Method for Microphysical Retrieval in Rain Using GPM Dual-Wavelength Radar, Journal of Atmospheric and Oceanic Technology, 33, 2205–2223, https://doi.org/10.1175/jtech-d-16-0020.1, 2016.

Jaffrain, J. and Berne, A.: Experimental Quantification of the Sampling Uncertainty Associated with Measurements from PARSIVEL Disdrometers, Journal of Hydrometeorology, 12, 352–370, https://doi.org/10.1175/2010jhm1244.1, 2011.

Kozu, T., Nakamura, K., Meneghini, R., and Boncyk, W.: Dual-parameter radar rainfall measurement from space: a test result from an aircraft experiment, IEEE Transactions on Geoscience and Remote Sensing, 29, 690–703, https://doi.org/10.1109/36.83983, 1991.

Kummerow, C., Mack, R. A., and Hakkarinen, I. M.: A Self-Consistency Approach to Improve Microwave Rainfall Rate Estimation from Space, Journal of Applied Meteorology, 28, 869–884, https://doi.org/10.1175/1520-0450(1989)028<0869:ascati>2.0.co;2, 1989.

Mardiana, R., Iguchi, T., and Takahashi, N.: A dual-frequency rain profiling method without the use of a surface reference technique, IEEE Transactions on Geoscience and Remote Sensing, 42, 2214–2225, https://doi.org/10.1109/tgrs.2004.834647, 2004.

Marshall, J. S. and Palmer, W. M. K.: THE DISTRIBUTION OF RAINDROPS WITH SIZE, Journal of Meteorology, 5, 165–166, https://doi.org/10.1175/1520-0469(1948)005<0165:tdorws>2.0.co;2, 1948.

Marzoug, M. and Amayenc, P.: A Class of Single- and Dual-Frequency Algorithms for Rain-Rate Profiling from a Spaceborne Radar. Pad I: Principle and Tests from Numerical Simulations, Journal of Atmospheric and Oceanic Technology, 11, 1480–1506, https://doi.org/10.1175/1520-0426(1994)011<1480:acosad>2.0.co;2, 1994.

Meneghini, R., Kozu, T., Kumagai, H., and Boncyk, W. C.: A Study of Rain Estimation Methods from Space Using Dual-Wavelength Radar Measurements at Near-Nadir Incidence over Ocean, Journal of Atmospheric and Oceanic Technology, 9, 364–382, https://doi.org/10.1175/1520-0426(1992)009<0364:asorem>2.0.co;2, 1992.

Meneghini, R., Kumagai, H., Wang, J., Iguchi, T., and Kozu, T.: Microphysical retrievals over stratiform rain using measurements from an airborne dual-wavelength radar-radiometer, IEEE Transactions on Geoscience and Remote Sensing, 35, 487–506, https://doi.org/10.1109/36.581956, 1997.

https://doi.org/10.5194/egusphere-2023-2220
Preprint. Discussion started: 13 November 2023

Raupach, T. H. and Berne, A.: Correction of raindrop size distributions measured by Parsivel disdrometers, using a two-dimensional video disdrometer as a reference, Atmospheric Measurement Techniques, 8, 343–365, https://doi.org/10.5194/amt-8-343-2015, 2015.

Sauvageot, H. and Lacaux, J.-P.: The Shape of Averaged Drop Size Distributions, Journal of the Atmospheric Sciences, 52, 1070–1083, https://doi.org/10.1175/1520-0469(1995)052<1070:tsoads>2.0.co;2, 1995.

Sheppard, B. E.: Sampling Errors in the Measurement of Rainfall Parameters Using the Precipitation Occurrence Sensor System (POSS), Journal of Atmospheric and Oceanic Technology, 24, 125–140, https://doi.org/10.1175/jtech1956.1, 2007.

Tokay, A., Kruger, A., and Krajewski, W. F.: Comparison of Drop Size Distribution Measurements by Impact and Optical Disdrometers, Journal of Applied Meteorology, 40, 2083–2097, https://doi.org/10.1175/1520-0450(2001)040<2083:codsdm>2.0.co;2, 2001.

Ulbrich, C. W.: Natural Variations in the Analytical Form of the Raindrop Size Distribution, Journal of Climate and Applied Meteorology, 22, 1764–1775, https://doi.org/10.1175/1520-0450(1983)022<1764:nvitaf>2.0.co;2, 1983.

Waterman, P.: Matrix formulation of electromagnetic scattering, Proceedings of the IEEE, 53, 805–812, https://doi.org/10.1109/proc.1965.4058, 1965.

Williams, C., Bringi, V., Carey, L., Chandrasekar, V., Gatlin, P., Haddad, Z., Meneghini, R., Munchak, s., Nesbitt, S., Petersen, W., Tanelli, S., Tokay, A., Wilson, A., and Wolff, D.: Describing the Shape of Raindrop Size Distributions Using Uncorrelated Raindrop Mass Spectrum Parameters, Journal of Applied Meteorology and Climatology, 53, 1282–1296, https://doi.org/10.1175/JAMC-D-13-076.1, 2014.

Zhang, G., Vivekanandan, J., and Brandes, E.: A method for estimating rain rate and drop size distribution from polarimetric radar measurements, IEEE Transactions on Geoscience and Remote Sensing, 39, 830–841, https://doi.org/10.1109/36.917906, 2001.

https://doi.org/10.5194/egusphere-2023-2220
Preprint. Discussion started: 13 November 2023

Radars		
	RCWF	RCMD
Model	WSR-88D	Meteor 1700C
Peak Power	700 KW	250 KW
Operating Band	S-Band	C-Band
Wavelength	10.5 cm	5.3 cm
Longitude	121.7813° N	121.7728° E
Latitude	25.0714° N	25.0728° E
Beamwidth	0.93°	0.90°
Range Resolution	250 m	100 to 500 m
Minimum System PhiDP	60°	10°
PRF	320-1300 Hz	250-2000 Hz
VCP	221	82

Table 1. Technical specifications of two polarimetric radars (RCWF and RCMD) used in the current work.

https://doi.org/10.5194/egusphere-2023-2220
Preprint. Discussion started: 13 November 2023

PARSIVEL Disdrometer	
Manufacturer	OTT HydroMet
Sampling Area	50 cm^2
Drop Size Range	0.06-24.5 mm
Velocity Range	0.05-20.8 m/s

Table 2. Disdrometer Characteristics

https://doi.org/10.5194/egusphere-2023-2220
Preprint. Discussion started: 13 November 2023

Figure 1. RCMD (C-Band) left and RCWF (S-Band) right at the Wufenshan weather station

https://doi.org/10.5194/egusphere-2023-2220
Preprint. Discussion started: 13 November 2023

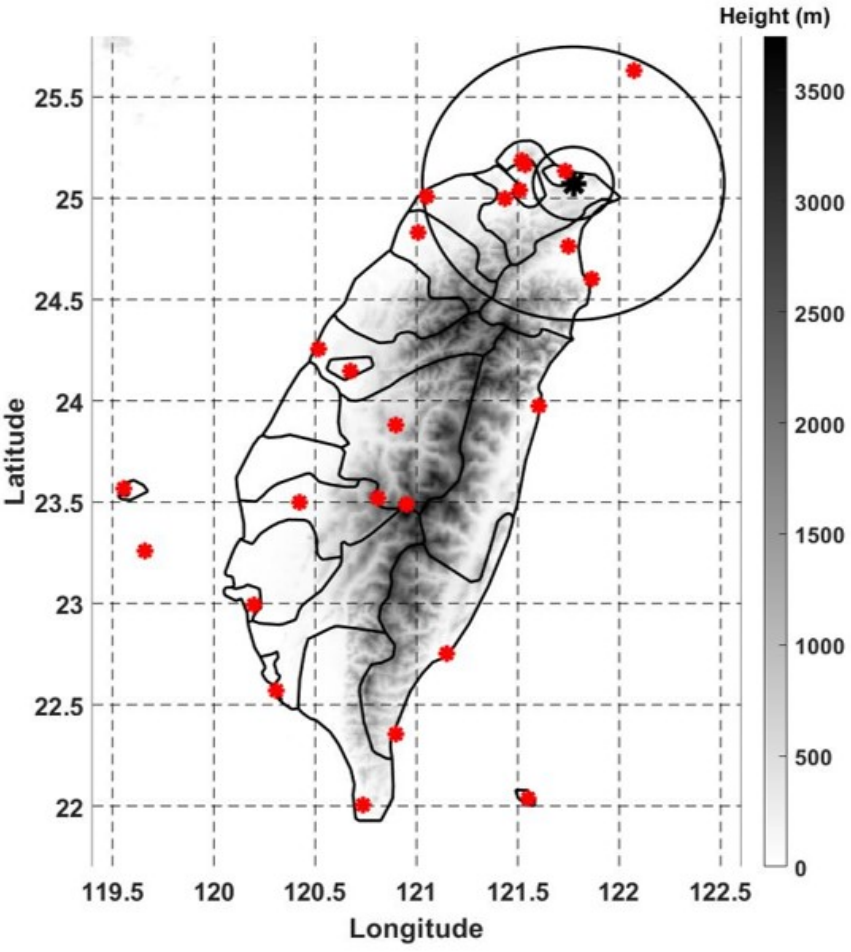

Figure 2. Taiwan - Instrument Locations. The radar site is shown by the solid black asterisk on the North. Circles with 25 km and 100 km radii are drawn around the location to indicate the data viability region. Measurement stations with disdrometers are shown in red. Terrain height is indicated in grayscale throughout the map for reference.

https://doi.org/10.5194/egusphere-2023-2220
Preprint. Discussion started: 13 November 2023

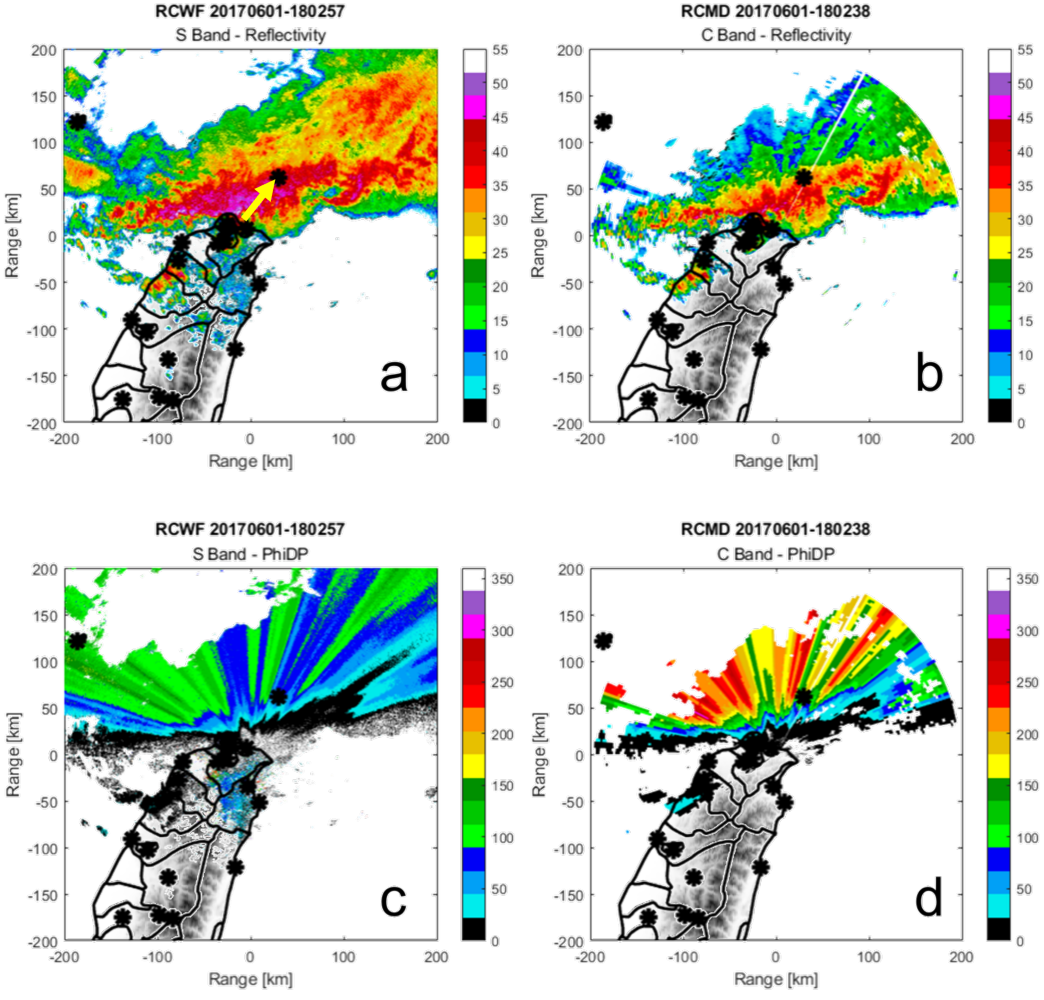

Figure 3. Panels a and b show the reflectivity measured in S-band and C-band respectively. The yellow arrow in panel a indicates the radial path from the radars to the disdrometer location of interest. Panels c and d contain the raw differential phase measurements recorded in S-band and C-band.

https://doi.org/10.5194/egusphere-2023-2220
Preprint. Discussion started: 13 November 2023

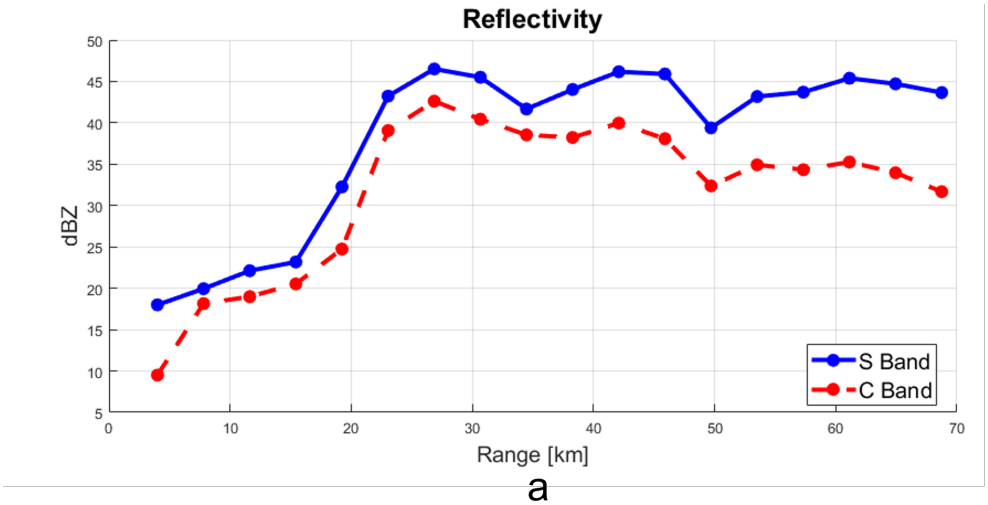

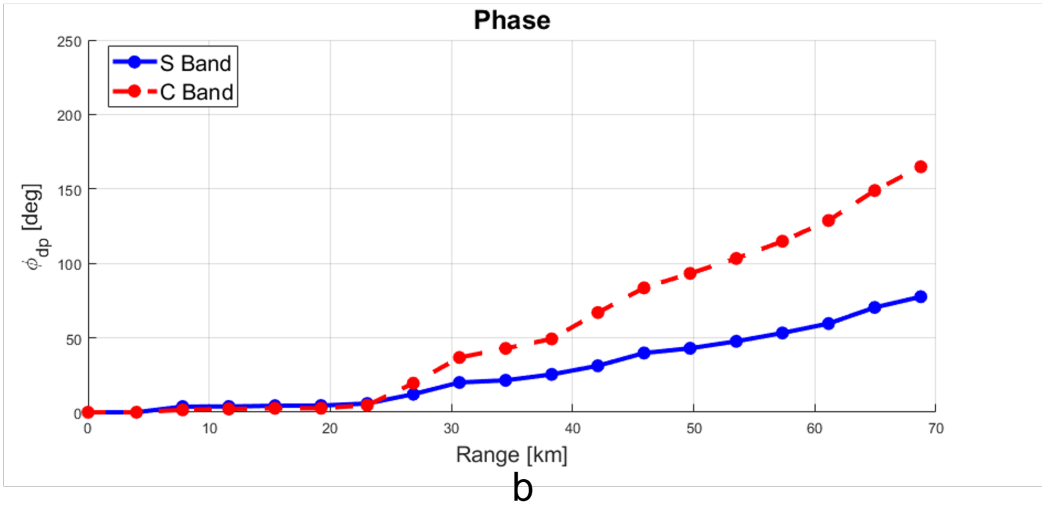

Figure 4. The data along the radial indicated in Figure 3 following preprocessing yields the reflectivity (a) and differential phase (b) used in the retrieval for this measurement time.

https://doi.org/10.5194/egusphere-2023-2220
Preprint. Discussion started: 13 November 2023

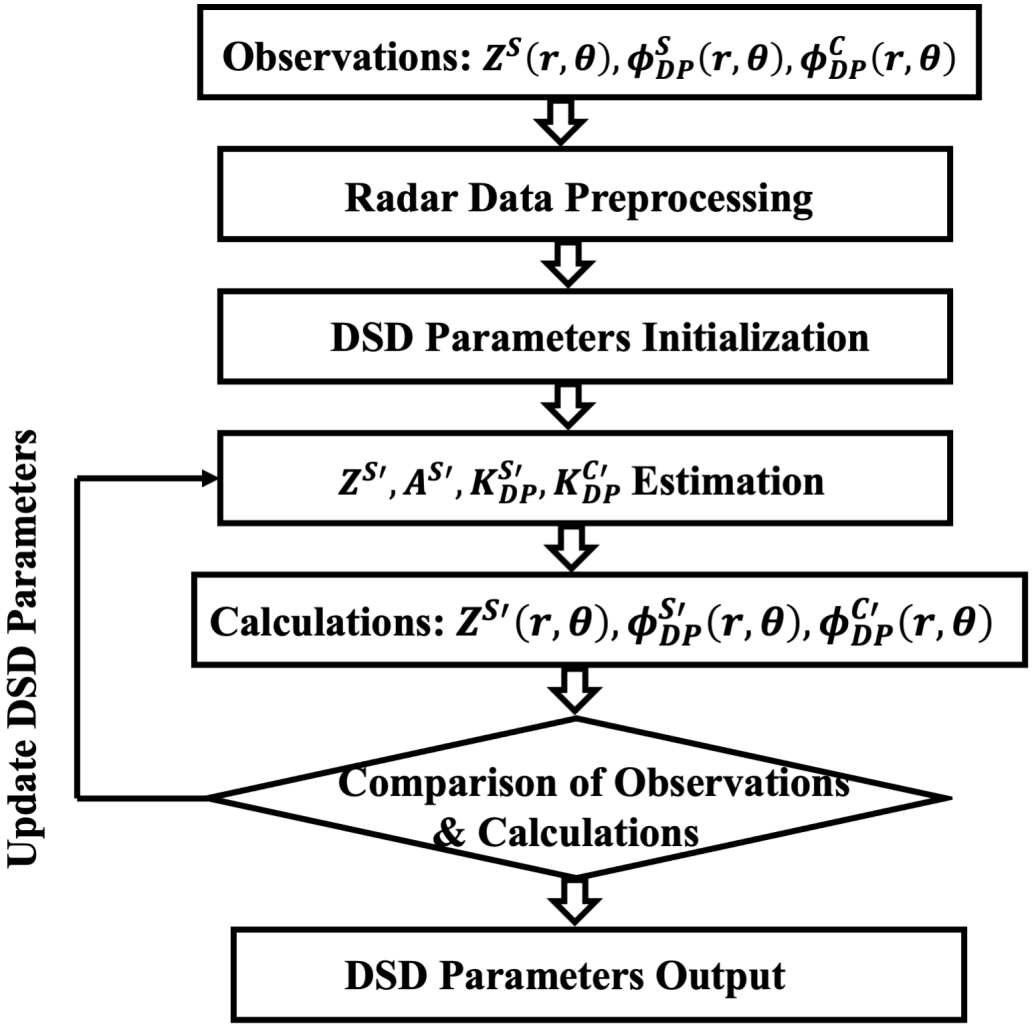

Figure 5. The algorithm applied to each gate seeks DSD parameters which produce reflectivity and estimated specific differential phase values that correspond to the radar reflectivity and differential phase values observed at the disdrometer location by RCMD and RCWF.

https://doi.org/10.5194/egusphere-2023-2220
Preprint. Discussion started: 13 November 2023

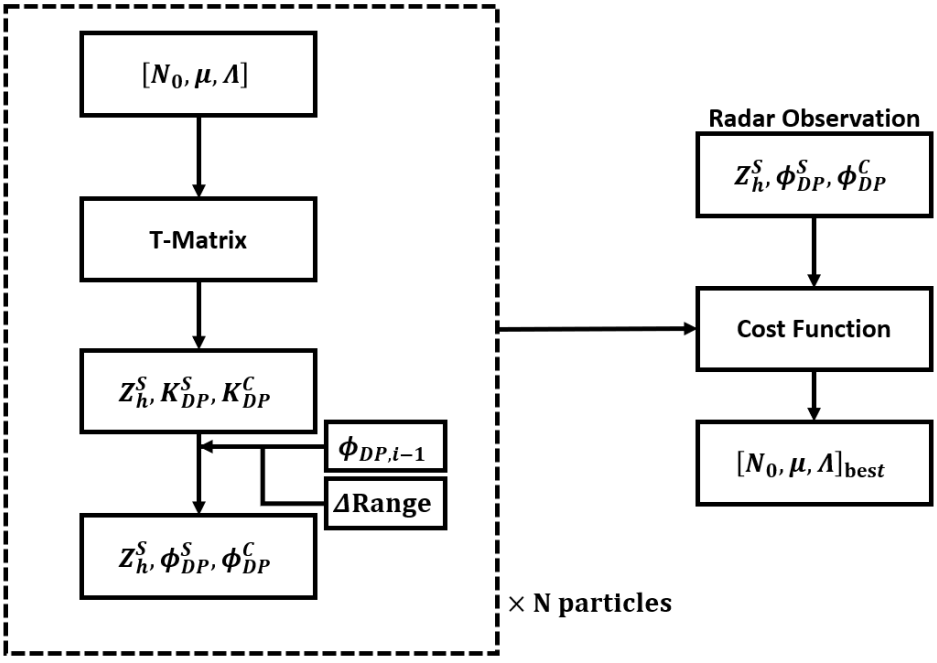

Figure 6. Particle Swarm Optimization for Gate of Interest. Each particle has an independent set of gamma distribution defining variables that is used to estimate reflectivity and specific differential phase values using the T-Matrix method. Range differentials and previously determined phase are used to produce estimated parameters which can then be applied to a cost function relative to the observed values.

https://doi.org/10.5194/egusphere-2023-2220
Preprint. Discussion started: 13 November 2023

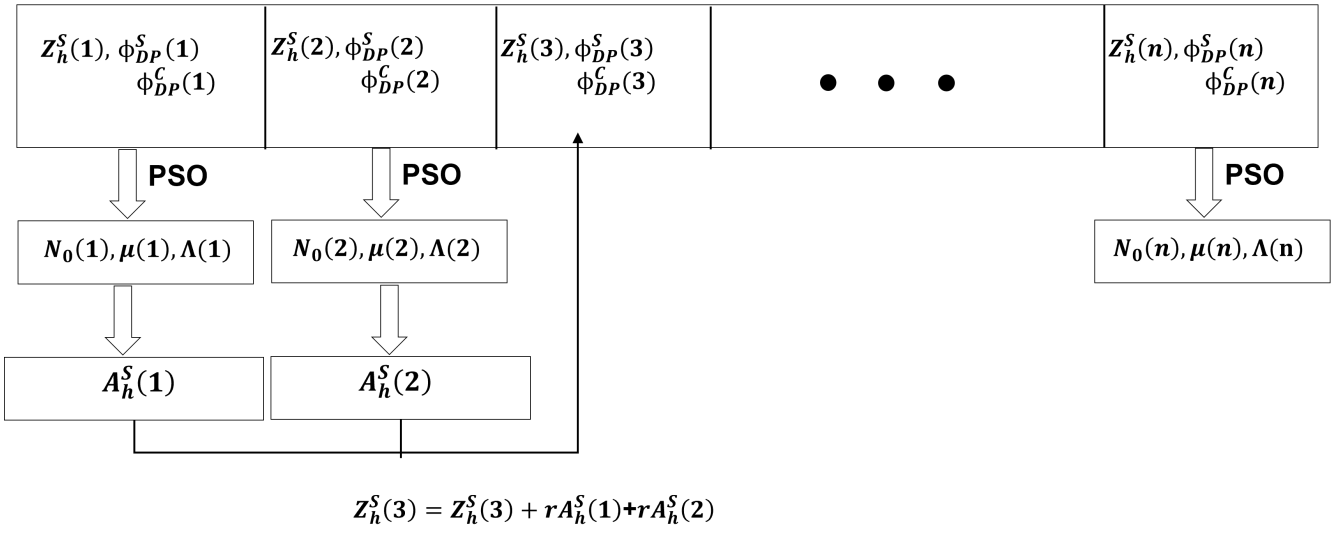

Figure 7. Retrieval Along Radial. The process begins with the first gate which is assumed to be unaffected by attenuation. The reflectivity and phase information serve as inputs to the PSO of each gate and produce DSD values that can be used to calculate the local attenuation. The next gate's observed reflectivity value is updated with any previously accumulated attenuation before being used in the next optimization. The process continues until the final gate's values are determined.

https://doi.org/10.5194/egusphere-2023-2220
Preprint. Discussion started: 13 November 2023

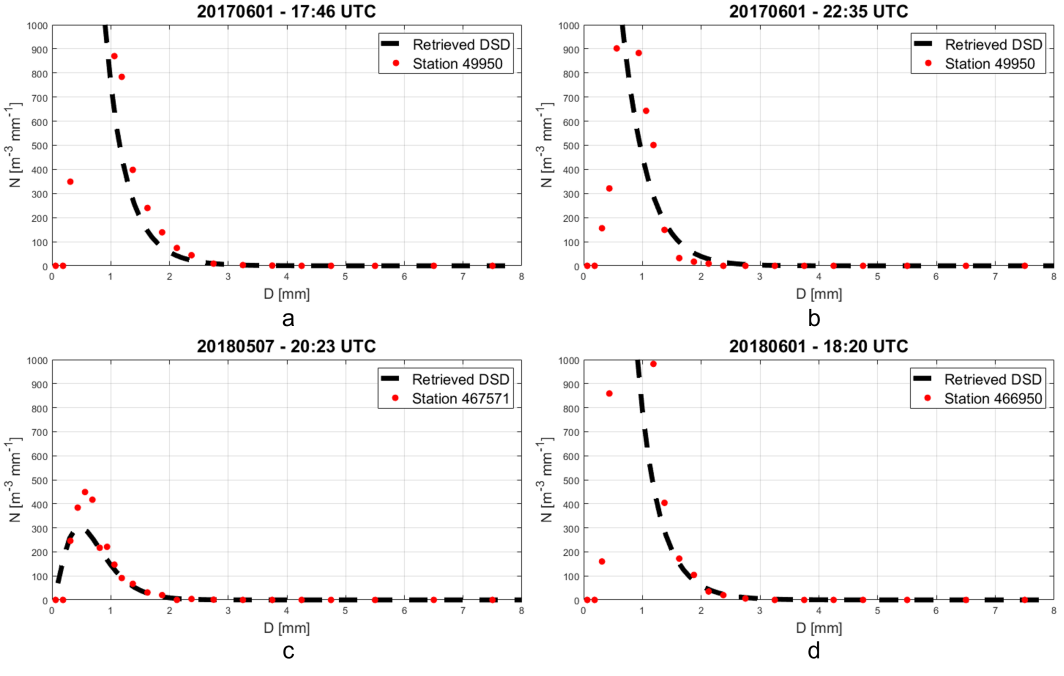

Figure 8. Panels a-d show four qualitative examples of the results achieved by the algorithm. Local disdrometer particle size concentrations are shown by the red markers of each plot while the algorithm's retrieval results are plotted with a black dashed line.

https://doi.org/10.5194/egusphere-2023-2220
Preprint. Discussion started: 13 November 2023

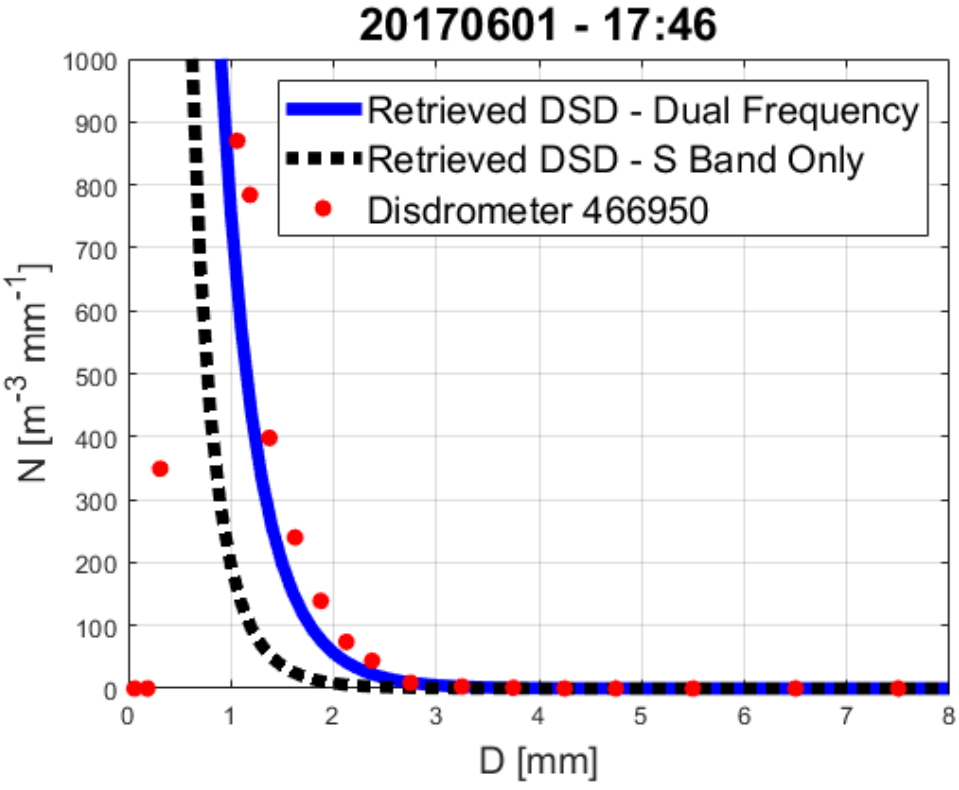

Figure 9. This example demonstrates the dual polarization/dual frequency approach represented by the solid blue line much more closely matches the disdrometer measurements shown with red markers. The black dashed line was produced by only using the dual polarization data from RCWF.

https://doi.org/10.5194/egusphere-2023-2220
Preprint. Discussion started: 13 November 2023

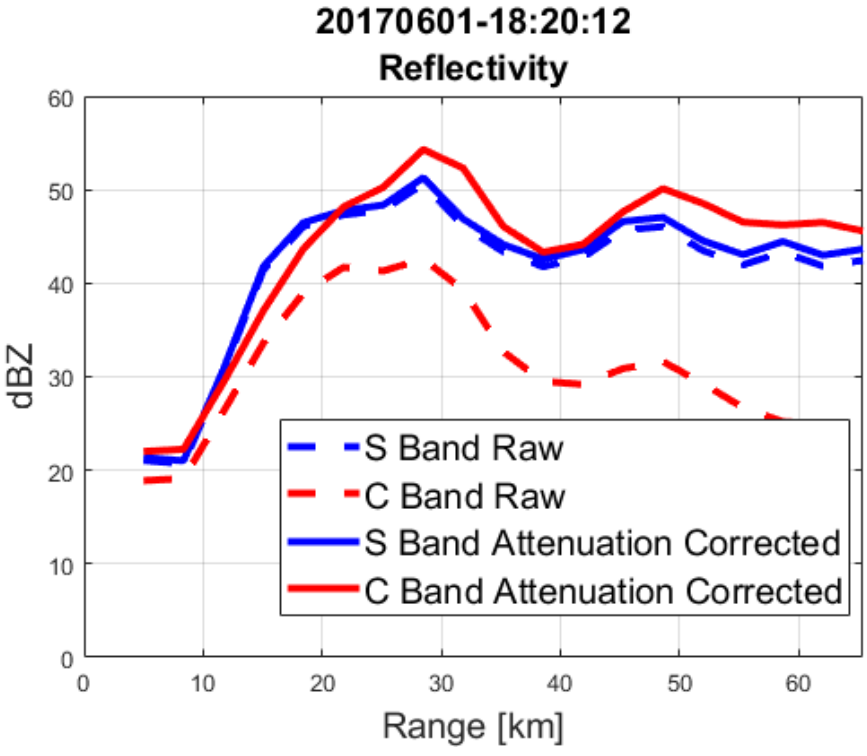

Figure 10. The S-band reflectivity is relatively unaffected by attenuation as presented by the raw reflectivity values shown with a dashed blue line and the attenuation-corrected reflectivity values indicated by solid blue. The corrected C-band reflectivities shown with red solid line match very well with the S-band values.